Camera-based experimental modal analysis with impact excitation: reaching high frequencies thanks to one accelerometer and random sampling in time

Yonggang Wang[a,b,c,*], Felix Simeon Egner[a,b], Thijs Willems[a,b], Matteo Kirchner[a,b], Wim Desmet[a,b]

[a] *KU Leuven, Department of Mechanical Engineering, Celestijnenlaan 300, B-3001, Leuven, Belgium*
[b] *DMMS lab, Flanders Make, Belgium*
[c] *SIM M3 program, Technologiepark 48, B-9052 Zwijnaarde, Belgium*

Abstract

Experimental Modal Analysis (EMA) allows to assess the dynamical properties of a mechanical component or structure by estimating the modal parameters. Whereas EMA is usually based on local accelerometers or laser vibrometer data, in this paper we focus on camera-based EMA as cameras offer full field and contact-less data. However, besides few very specific controlled cases, camera-based EMA is limited by the low frame rate of the camera in comparison to accelerometers and vibrometers. In this paper we propose a novel acquisition scheme that allows to estimate modal parameters above the Nyquist-Shannon limit (*i.e.*, half of the camera frame rate) by employing a random sampling scheme in time in combination with one accelerometer. With this information we reconstruct the Impulse Response Function (IRF) modal model through a nonlinear optimization problem, where the accelerometer ensures a global solution by providing an initial guess of the eigenfrequencies. We investigate numerically the accuracy of the methodology by simulating multiple damped sine waves. Furthermore, we present an experimental validation on a clamped-clamped beam excited by an impact hammer. Thereby, the displacement information is captured by a single camera triggered by random pulses, and computed by Lucas-Kanade (LK) optical flow. The complexity and modal assurance criterion (MAC) of the modes show that all modes whose amplitudes are higher than the noise level are measured successfully with only one excitation hit, where the highest mode, at $218\,\mathrm{Hz}$, is measured with a random sampling scheme comparable to $50\,\mathrm{fps}$ (to reach $218\,\mathrm{Hz}$, a regular sampling with $436\,\mathrm{fps}$ would be required).

Keywords: Random sampling, Nonlinear optimization, Camera measurements, Experimental modal analysis, Optical flow

*Corresponding author

Email addresses: yonggang.wang@kuleuven.be (Yonggang Wang), felix.egner@kuleuven.be (Felix Simeon Egner), thijs.willems@kuleuven.be (Thijs Willems), matteo.kirchner@kuleuven.be (Matteo Kirchner), wim.desmet@kuleuven.be (Wim Desmet)

1. Introduction

Modal parameters (eigenfrequencies, damping factors, mode shapes) reflect the dynamic properties of structures and are employed in various phases of the life cycle of mechanical systems. For example, they can be parameters in the design of structures to prevent resonance during operation, or for damage identification on structures [1, 2]. Modal analysis is a well-known experimental technique to determine the modal parameters, and can be divided into Experimental Modal Analysis (EMA) and Operational Modal Analysis (OMA). The main difference is that EMA requires the system excitation to be known (*e.g.*, impact hammer or shaker), whereas OMA can deal with an unknown and possibly also uncontrolled excitation. Therefore, OMA is preferred when measuring the excitation is difficult or when operational conditions strongly influence the dynamics [3, 4, 5, 6], whereas EMA is well suited to a lab environment, and is more reliable for damping estimation [7, 8, 9].

Both techniques require the measurement of the system response, and a common choice is to employ accelerometers, which provide information at discrete points. However, accelerometers have the drawback that their additional mass may impact the dynamic behavior of the system. A spatially dense mode shape can be obtained by an overwhelming number of sensors or by multiple excitation (roving excitation, which is time consuming). Alternatively, non-contact methods count on Laser Doppler Vibrometry (LDV) [10], Electronic Speckle Pattern Interferometry (ESPI)[11], *etc.* LDV is limited to steady excitation as multiple points need to be measured by a scanning system, whereas the optical setup of ESPI is complex because the object and reference laser beam need to be aligned to measure their phase difference.

Cameras can provide spatially dense information for modal analysis, do not require any scanning system (and thus camera-based EMA is not limited to steady-state excitation), and consist of a simple optical setup, making them appealing in comparison with LDV and ESPI. In contrast to accelerometer-based and vibrometer-based modal analysis (which process acceleration and velocity, respectively), cameras capture displacement data by tracking the displacement of an object through the variation of the image intensity, with the help of image processing algorithms [12, 13]. For example, Phase-based Motion Magnification (PMM) aims to visualize and measure movement through phase measurements [14, 15]. Compared with intensity-based method, it is robust to illumination changes but requires setting kernel functions to calculate the phase of the image subset. Digital Image Correlation (DIC) measures displacements as well as strains via image subset correlation [16]. The correlation function in DIC involves an affine transformation model, hence extra computation time is needed in comparison with the translation-only model. Concerning displacement-only measurements, Lucas-Kanade (LK) optical flow simplifies the correlation function in DIC into the translation-only model. LK is valid under the assumption that the deformation is negligible compared to the translation and the overall brightness is constant [17, 18, 19]. OMA [5, 6, 20] and EMA [21, 22] can be performed on the outcome of camera-based displacement measurements.

Compared with an accelerometer, the sampling frequency (frame rate) of a camera is generally much lower. For instance, a typical frequency range of piezoelectric accelerometers is $1\,\mathrm{Hz}$ to $10\,000\,\mathrm{Hz}$ [23], whereas the frequency range for microelectromechanical or optomechanical accelerometers technology is usually higher[24]. In contrast, a typical high-speed camera operates at a frame rate of around $1000\,\mathrm{fps}$ (frames per second)[25], whose in-plane and out-of-

plane displacement accuracies are approximately 0.01 pixel and 0.03 pixel, respectively [26, 27]. Cameras with a high frame rate are expensive, and there is a trade-off between the frame rate and spatial resolution. When the frame rate is too low, two different sine waves may have the same value at the sampling points. This issue is called aliasing and can be avoided by applying a low-pass filter. For example, we can set a long exposure time of the camera, and the light intensity variation from high frequency vibration will be averaged and filtered out [28].

Various works aim to improve the frequency range in the camera-based modal analysis. If a camera with a rolling shutter is utilized, column pixels (or row pixels depending on the orientation) in the image are recorded sequentially, offering the possibility to exploit the phase shifts of different columns to measure natural frequencies which are higher than the camera frame rate [29]. However, most industrial cameras (including the camera used in this paper) have a global shutter (*i.e.*, they take a snapshot of the entire scene at a single time instant), which is also favorable for the LK optical flow. In the specific case of a vibration signal dominated by a known single frequency component, aliasing can be exploited in order to remap the high frequency signal to the low frequency band thus can be measured with a low sampling frequency [16]. However, if the frequency of vibration is unknown, low sampling frequency is problematic, and data processing algorithms are used to recover frequency content higher than the Nyquist frequency. For instance, Blind Source Separation (BSS) for OMA [6, 30] can separate displacements in a wide frequency band into individual modal coordinates and extract the modal parameters from a randomly re-sampled video. Moreover, OMA can also be performed with compressed data via a power spectrum blind multi-coset sampling approach [31]. In the case of the free vibration without damping, Atomic Norm Minimization (ANM) can estimate mode shapes and eigenfrequencies from random temporal compressed data[32, 33], and Singular Value Decomposition (SVD) can also be used to obtain mode shapes from randomly compressed measurements [34]. Previous works about BSS, ANM and SVD prove the feasibility of reducing the averaged sampling frequency of the camera by random re-sampling and then recovering the modal response of the structure. This feasibility motivates us to utilize random sampling as a data acquisition method to handle the sub-Nyquist sampling frequency in the case of EMA on a damped structure.

Random sampling has been investigated in the field of Compressive Sensing (CS) since 2006 [35, 36, 37]. A basic requirement in CS is that the measured signal can be represented by nearly orthogonal bases. Various CS-based frameworks have been proposed to recover the compressed sparse data, e.g. re-weighted basis pursuit de-noising [38] and group sparse optimization [39] with Discrete Fourier Transform (DFT) orthonormal basis. The orthonormal property is characterized by the Restricted Isometry Property (RIP) [40, 41], but the RIP is difficult to meet in the modal space. To recover higher frequency content than the Nyquist frequency without the RIP, J. Javh et al. excited the structure in a predetermined frequency band. After repeating the measurements in various frequency bands and merging these frequency bands, they demonstrated the advantageous use of aliasing for measurements above the Nyquist frequency [42]. Similarly, in time domain, if the signal is repeatable and its phase is manipulable, repetitions with different phases are also a feasible approach [43]. When the illumination is modulated harmonically, high frequency content related to the harmonic light can also be measured by using Fourier integrals. By changing the frequency of the light, other frequency content can be measured [44]. Nev-

ertheless, the repetition of measurements is time-consuming, and the requirement of having a repeatable excitation signal also limits the application of these approaches.

To improve the camera's frequency bandwidth in the modal space, thus going beyond the Nyquist-Shannon sampling frequency, in this paper we propose a time domain random sampling acquisition scheme and subsequent modal sparse recovering for the case of impact excitation. The dynamical response to an impact is considered as a combination of damped sine waves, which can be regarded as basis. The implementation details are described in the upcoming sections. Section 2 introduces camera-based EMA and the LK optical flow algorithm. Section 3 elaborates on the practicalities of random sampling with restricted sampling time interval of the camera, and on the optimization method to recover the modal response from the randomly sampled data. Section 4 evaluates the accuracy of optimization with simulated randomly sampled data. Section 5 shows an experimental application on a clamped-clamped beam and discusses the experiment results. Section 6 concludes this paper and discusses possibilities for future research.

2. Camera-based EMA and image processing algorithms

In this section, the basics of EMA are illustrated in section 2.1, followed by details on camera-based displacement measurement in section 2.2 and the procedure of camera-based EMA in section 2.3.

2.1. Basics of EMA

Fig. 1 shows the workflow of EMA in the case of accelerometer measurements, requiring a Data Acquisition Systems (DAS) to record the system input (hammer force) together with the acceleration (Acc.) signals. These signals are used to estimate the Frequency Response Functions (FRFs), which constitute the foundation of EMA [23]. The system can also be excited in a controlled way by a shaker. However, in this paper we only consider hammer excitation since an impact force results in a constant power spectral density (within a certain frequency range depending on the range of interest and the hardness of the hammer tip [23]). An impact force can also easily be represented in the random sampling model.

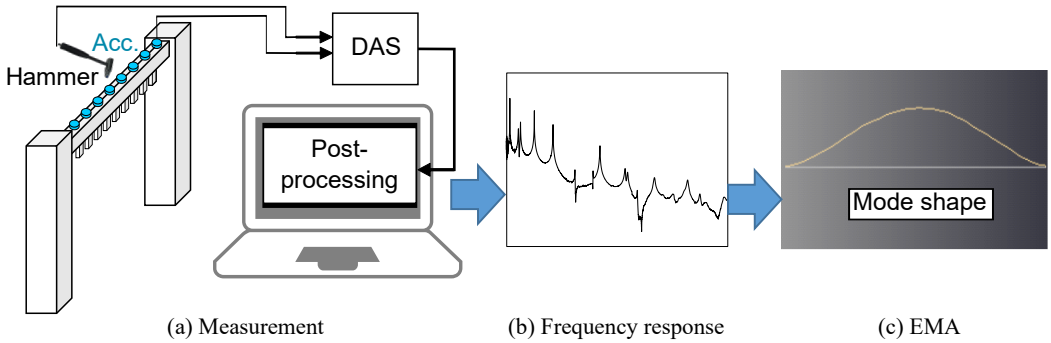

(a) Measurement (b) Frequency response (c) EMA

Figure 1: Procedure of conventional EMA.

To estimate the modal parameters, we require a modal model as described in frequency domain by eq. (1) [23].

$$
\begin{aligned}
H(j\omega) &= \sum_{i=1}^{N} \left(\frac{L_i \psi_i^{\top}}{j\omega - \lambda_i} + \frac{L_i^* \psi_i^{*\top}}{j\omega - \lambda_i^*} \right) + UR - \frac{LR}{\omega^2} \\
X(j\omega) &= H(j\omega) F(j\omega)
\end{aligned}
\tag{1}
$$

$H(j\omega)$ is the estimated FRF, $L_i = Q_i \psi_i$ are modal participation factors and represent the interaction between modes and excitation, where Q_i is a scaling factor and ψ_i is a modal vector. $\lambda_i = -\sigma_i + j\omega_i$ are (complex) poles, and depend on the damping and on the eigenfrequency of their correspondent mode. Superscript $^{\top}$ and * are the transpose and complex conjugate, respectively. LR and UR are the lower and upper residual terms, and are used to approximate the effects of modes outside the frequency range of interest. The vibration output $X(\omega)$ is obtained by multiplying the system input $F(j\omega)$ and the FRF $H(j\omega)$. FRFs and modal model allow to estimate the modal parameters, where the PolyMAX method can be used to obtain stabilization diagrams and therefore to select the modes [45].

PolyMAX consists of two steps, the LSCF (Least-Squares Complex Frequency) step and the LSFD (Least-Squares Frequency Domain) step. LSCF starts from a right matrix-fraction model [46, 47]. Fitting the fraction model with experimental FRFs yields several system poles among which consistent and stable poles (λ_i) have to be selected by making use of the stabilization diagram [48]. This procedure can be automatized by introducing stabilization tolerances [48]. In the LSFD step, the mode shapes are obtained by estimating the modal vectors ψ_i and scaling factors Q_i with the selected λ_i and corresponding L_i.

Besides working in frequency domain with the above mentioned FRFs, the dynamic response of a structure can be represented in the time domain by Impulse Response Functions (IRFs) $h(t_s)$, which are the inverse Fourier transforms of $H(j\omega)$ without the residual terms.

$$
\begin{aligned}
h(t_s) &= \sum_{i=1}^{N} \left(Q_i \psi_i \psi_i^{\top} e^{\lambda_i t_s} + Q_i^* \psi_i^* \psi_i^{*\top} e^{\lambda_i^* t_s} \right) \\
x(t_s) &= h(t_s) * f(t_s)
\end{aligned}
\tag{2}
$$

$h(t_s)$ is a sum over the modal contributions indicated by the mode number i. The convolution of the system input $f(t_s)$ and the IRFs $h(t_s)$ leads to the vibration output $x(t_s)$ of the system in time domain. The time vector t_s has a constant time step in the case of regular sampling, whereas in section 3.2 we will discuss how to deal with the proposed irregular sampling scheme (where the time time steps are generated by a uniformly distributed random variable).

2.2. Camera-based displacement measurements

When working with cameras, the first step is a calibration to define the projection from the 3D scene to 2D pixel coordinates (fig. 2), which is represented by the camera projection matrix ($P = K[R| - RC]$). Here, $[R| - RC]$ is the extrinsic matrix and represents the translation

and rotation between the 3D scene and the camera plane, whereas K is the intrinsic matrix consisting of scaling factors and axis shift from the camera plane to the sensor plane. P is computed thanks to a few pictures of a checkerboard pattern with known dimensions taken at different orientations, whose corners are detected by image processing algorithm [49].

Furthermore, lens distortions can be taken into account to improve measurement accuracy within the whole field of view. This involves higher order terms in the projection matrix [50] instead of a linear approximation, and hence it is more accurate.

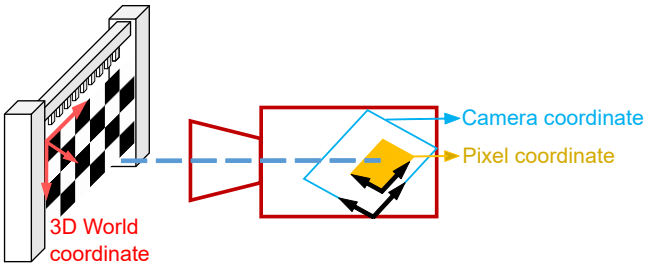

Figure 2: Projection in camera calibration.

Once all calibration parameters are known, the measurements of the vibrating structure can take place. Markers (*e.g.*, checkerboards, dots, speckle pattern) can be attached or printed on the specimen under investigation to create sufficient high-contrast feature points (*e.g.*, a sharp corner). Natural feature points on the specimen are also applicable but may not be ubiquitous. Each frame of the video needs to be corrected by the calibration parameters, after which various image processing algorithms (some examples were mentioned in the introduction) can be used to measure the displacement at the points of interest. This can involve a single camera or multiple views (*e.g.*, stereo camera) depending on the application. In this paper we adopt a single camera since we are interested in the vibrations of a beam in a single plane. In case of a stereo vision system, an extra step is required to match the feature points from each camera such that 3D displacements can be calculated by triangulation [16].

In this paper we adopt the Lucas-Kanade (LK) optical flow method to track the displacements, because it is well suited for sub-pixel displacement estimation. The LK optical flow has a simple objective function and is fast in computation in comparison with other tracking methods [17]. Its basic idea is to minimize the difference of tracked image subsets in two frames (fig. 3):

$$\arg\min_{u,v} E = \sum_{\Omega} \left[I(x+u, y+v, t+1) - I(x,y,t) \right]^2 \tag{3}$$

where $I(x,y,t)$ are gray levels within Ω in the current frame, and $I(x+u, y+v, t+1)$ are gray levels within Ω in the next frame. Ω indicates an image subset around the tracked point. E is the Sum of Squared Differences (SSD) of the subsets gray levels. x, y represent the position of the tracked point, whose displacement is u, v during the tracking.

An interpolation of $I(x+u, y+v, t+1)$ is required to get a continuous function and thus allowing to calculate the displacement $\begin{bmatrix} u & v \end{bmatrix}$ at sub-pixel level, and this is usually implemented in form of a locally convex cubic function [17]. To find the minimum of the objective function in eq. (3), we adopt a linear approximation $I(x,y,t) + I_t + \begin{bmatrix} u & v \end{bmatrix} \begin{bmatrix} I_x & I_y \end{bmatrix}^\top$ of $I(x+u, y+v, t+1)$,

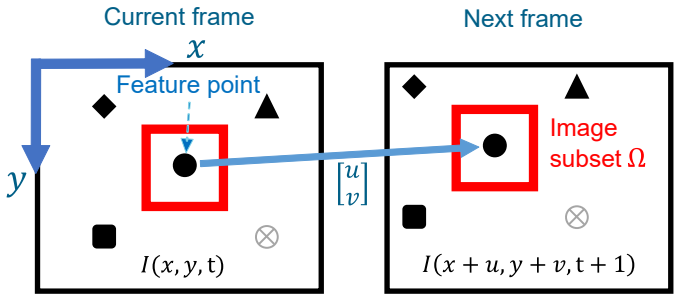

Figure 3: Principle of the Lucas-Kanade optical flow.

where I_t is the temporal derivative and I_x, I_y are spatial gradients of the image, and pursuit to make $\begin{bmatrix}\partial E/\partial u & \partial E/\partial v\end{bmatrix}^\top = 0$. Other numerical methods are discussed in [17].

Consequently, the displacement of the image subset $\begin{bmatrix}u & v\end{bmatrix}$ can be calculated as:

$$\begin{bmatrix}u\\v\end{bmatrix} = \begin{bmatrix}I_x^2 & I_xI_y\\I_yI_x & I_y^2\end{bmatrix}^{-1}\begin{bmatrix}-I_tI_x\\-I_tI_y\end{bmatrix} \tag{4}$$

To minimize the linearization error, we apply an iterative calculation of $\begin{bmatrix}u & v\end{bmatrix}$, where the initial guess of $\begin{bmatrix}u & v\end{bmatrix}$ in the next iteration comes from the current output of the calculation. This linear approximation method tracks feature points individually and thus is a subset-based local approach. The external factors may impact the success of tracking (*e.g.*, a periodic pattern within the image subset, image noise, light conditions and motion blur). Otherwise, we can adjust the experimental setup to avoid external factors (*e.g.*, modify the image subset size, increase the image resolution, apply additional light sources, set a proper exposure time).

2.3. Camera-based EMA

Camera-based EMA follows the same workflow of EMA, where displacement measurements are used instead of acceleration or velocity (fig. 1). For a single frequency, (*i.e.*, a damped sine wave), the displacement amplitude relates to the acceleration by the square of the angular frequency, while its phase shifts by π and the damping factor remains the same. Mathematically, $\mathcal{F}(x) = \mathcal{F}(\alpha)/(j\omega)^2$, where $\mathcal{F}$ indicates the Fourier transform, and x and $\alpha = \mathrm{d}^2x/\mathrm{d}t^2$ are displacement and acceleration, respectively.

The camera-based EMA workflow is summarized in fig. 4. The structure is excited by a hammer or a shaker, and at the same time displacements information are acquired by a camera and processed as described in section 5 (fig. 4(b)). Moreover, the excitation signal is measured by an impedance head (at the hammer tip or at the shaker), and afterwards the FRFs are calculated. Finally, the modal parameters are estimated using *e.g.* the PolyMAX method [45]. An example is given in section 5.

3. Random sampling in time and optimization model

Although camera-based EMA offers spatially dense data without the influence of the accelerometers mass in comparison with accelerometer-based EMA, it is generally limited by the

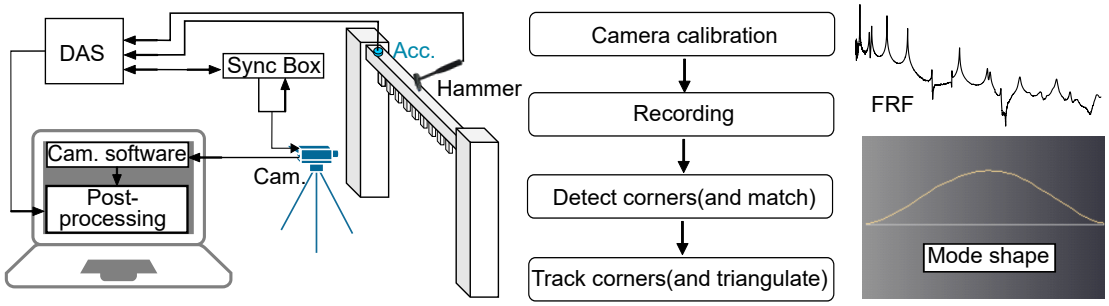

(a) Experiment (b) Image processing (c) EMA

Figure 4: Procedure of camera-based EMA.

frame rate of the camera. Our proposed methodology for camera-based EMA aims at going beyond the Nyquist-Shannon sampling frequency, *i.e.*, we want to estimate mode shapes above the frequency limit equal to half the camera's frame rate. To capture the necessary high frequency information, we propose to use a random sampling scheme [35].

Firstly, section 3.1 describes the procedure of conducting random sampling with a camera. Secondly, section 3.2 builds an optimization model to recover high frequency modal responses from randomly sampled vibrations. Finally, section 3.3 analyzes the feasibility of the optimization to find the global minimum of the objective function.

3.1. Sampling strategy

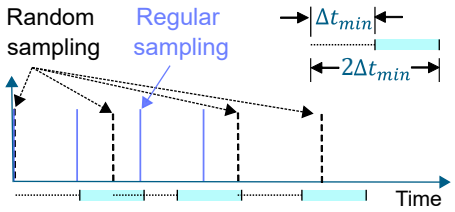

Figure 5: Random sampling of the camera frames.

Time data signals are usually regularly sampled at a predefined frame rate. In fig. 5 the highest frame rate of the camera ($1/\Delta t_{min}$) in regular sampling is limited by the exposure time and data transfer rate. According to the Nyquist-Shannon sampling theorem in regular sampling, the highest frequency of signals we can measure without aliasing is $1/(2\Delta t_{min})$. In the random sampling, the ambiguity in aliasing is eliminated, and two different sine waves have distinct values. Therefore, reconstruction of the higher frequency signal than $1/\Delta t_{min}$ is feasible.

To apply a random sampling acquisition scheme, we randomly trigger the camera. Due to the limitation of the frame rate, the time interval between two consecutive frames cannot exceed Δt_{min}. On the other hand, we want to acquire sufficient frames, and thus we set a maximum interval to $2\Delta t_{min}$. Therefore, the resulting trigger for the camera is between Δt_{min} and $2\Delta t_{min}$ (shown by the dashed lines in fig. 5), and the sampling interval Δt is then a continuous random

variable uniformly distributed on the interval $[\Delta t_{min}, 2\Delta t_{min}]$, *i.e.*, $\Delta t \sim U(\Delta t_{min}, 2\Delta t_{min})$, where U represents the continuous uniform distribution.

3.2. Optimization model of random sampling

To reconstruct high frequency modal responses, the IRF model needs now to be applied on the randomly sampled signal. Similar to the regularly sampled IRF model in eq. (2), the IRF in random sampling is $h(t) = \sum_{i=1}^{N} \Re(A_i e^{\lambda_i t})$, where the time vector is changed from t_s in eq. (2) to t, and Q_i and ψ_i are represented by a complex amplitude A_i at every sampling point in space. Both A_i and λ_i are complex numbers, and consequently $A_i = \Re(A_i) + \Im(A_i)j$ can also be represented as $A_i = a_i e^{j\varphi_i}$, where a_i is the amplitude and φ_i is the phase of mode i. Finally, $\lambda_i = 2\pi f_i j - \sigma_i$ consists of the frequency f_i and the damping σ_i of mode i.

The IRF indicates that the displacement response of a mechanical component can be decomposed into damped sine waves also in case of random sampling. If we substitute the IRF with random sampling into eq. (2), where the convolution of the IRF and the excitation equals to the measured response, their difference is expected to be zero. Therefore, we can minimize the squared residual to obtain A_i and λ_i:

$$\underset{A_i,\lambda_i}{\arg\min} \sum_{t} \left[\sum_{i=1}^{N} \Re(A_i e^{\lambda_i t}) * f(t) - y(t) \right]^2 - \varepsilon \tag{5}$$

where $f(t)$ is the excitation signal, N is the number of eigenfrequencies, ε is a constant number representing a possible offset, and $y(t)$ is the measured response. In this paper, the rigid body motion is not analyzed, thus the rigid body motion term is not included in eq. (5), which makes eq. (5) only applicable to the clamped-clamped boundary conditions because the rigid body motion is negligible in this case. Expansion of the current model to include general boundary conditions is one of our future steps, since it is possible to distinguish deformation from the rigid body motion or decompose the rigid body motion into damped sine waves.

The solution of the least square problem in eq. (5) followed by a modal analysis can be used to recover the complete modal response. Equation (5) is applicable to different excitation types. In fact, by substituting the measured excitation signal $f(t)$ in time domain into eq. (5), we can still optimize A_i and λ_i by time convolution. Nevertheless, if we assume an impact excitation, the IRF equals the measured response without the convolution operation, and thus the optimization takes less computation time compared with other excitation types. Moreover, choosing a shaker excitation is beneficial in case of high damping, as the impulse response would quickly decay to the noise level of the measurements.

3.3. Feasibility of the optimization problem in eq. (5)

Eq. 5 is a nonlinear optimization problem, whose solution can be obtained via a gradient-based algorithm with warm start. To analyze the feasibility of the optimization, we can investigate the convexity of the objective function $g(A_i, \lambda_i)$, *i.e.*, the deviation between a fitted sum of damped sine waves and the measured response. Meta-heuristic algorithms may also be employed to optimize the problem with less strict requirements on convexity, but they were not chosen here as they can end up into local optima [51]. Future research may further investigate this aspect.

As this paper focuses on impact excitation (and consequently $f(t)$ is an impulse function), we have simulated a measured response as as a damped sine wave, *i.e.*, $y(t) = \Re(e^{2\pi jt - t})$, and consequently eq. (5) becomes:

$$g(A_i, \lambda_i) = \sum_t \left[\sum_{i=1}^{N} a_i e^{-\sigma_i t} \cos(2\pi f_i t + \varphi_i) - e^{-t} \cos(2\pi t)) \right]^2 - \varepsilon \tag{6}$$

The solutions $A_i^\star, \lambda_i^\star$ of $g(A_i, \lambda_i)$ satisfy the definition of the local minimum:

$$\nabla^2 g(A_i^\star, \lambda_i^\star) \succeq 0, \nabla g(A_i^\star, \lambda_i^\star) = 0 \tag{7}$$

To analyze the feasibility of obtaining $A_i^\star, \lambda_i^\star$ by a gradient-based algorithm, we visualize how the objective function $g(A_i, \lambda_i)$ changes with respect to perturbations of A_i, λ_i, as shown in fig. 6. Regarding the damping, the real and imaginary parts of A_i, $g(A_i, \lambda_i)$ are globally quasiconvex, *i.e.*, along any segment in the error curve the highest point is one of the endpoints. Concerning the frequency, the error curve is only locally quasiconvex when the curve segment is close to the global minimum [52]. In other words, for any $\theta \in [0, 1]$ and for any frequency interval $[f_l, f_r]$ which is close to the global minimum, $g|_{f_i = \theta f_l + (1-\theta) f_r} \leq \max\left\{ g|_{f_i = f_l}, \quad g|_{f_i = f_r} \right\}$ holds [52].

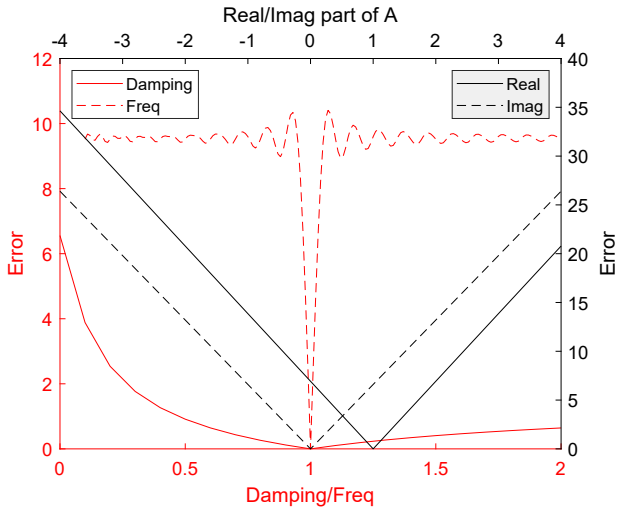

Figure 6: Objective function $g(A_i, \lambda_i)$ under perturbations of the variables.

Before starting the iterative search, if an initial guess of the frequency γ_i which lies in the local quasiconvex segment is provided, a global minimum is achievable by using a gradient-based solver. In this paper, a trust-region-reflective algorithm [53] is adopted, where the step size and search direction are calculated based on the gradient of the objective function. To improve the reproducibility of the optimization, some stopping criteria can be set, *e.g.*, a lower bound on the change of step size and a lower bound on the objective function during iteration, which in this paper are set to 1×10^{-6} and 1×10^{-10} , respectively. In general, these values are case-dependent and should not be lower than the precision of floating-point numbers in order to

avoid the risk of convergence issues. The initial guess of the eigenfrequencies can be obtained from an accelerometer, which can measure the eigenfrequencies at a higher frequency than the camera.

The objective function in eq. (6) (for a single damped sine wave) can be decomposed into a series of operations as shown in fig. 7. For multiple damped sine waves ($i > 1$) the preservation of quasiconvexity is not guaranteed, and consequently a local minimum is not always a global minimum (cf. eq. (7)). In signal processing this indicates aliasing, where the proposed random sampling scheme can eliminate the ambiguity happening in aliasing, thus making it possible to differentiate the contribution of each damped sine waves have in the summation $\sum_i$.

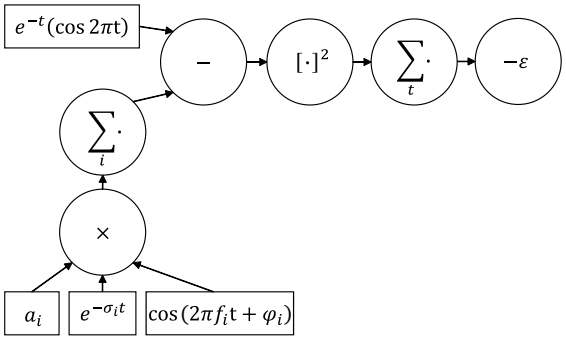

Figure 7: Expression tree of eq. (6).

Because of the local quasiconvexity over the frequency, the bound $\Delta\gamma_i$ of the frequency γ_i is set as a value close to the global minimum. Therefore, we add a constraint to eq. (5), and the final version of the optimization model is:

$$\begin{aligned} &\arg\min_{A_i,\lambda_i} \sum_t \left[\sum_{i=1}^{N} \Re(A_i e^{\lambda_i t}) * f(t) - y(t)\right]^2 - \varepsilon \\ &\text{s.t. } \gamma_i - \Delta\gamma_i \leq \Im(\lambda_i)/(2\pi) \leq \gamma_i + \Delta\gamma_i, i = 1, \ldots, N \end{aligned} \tag{8}$$

The global minimum is thus achieved when the initial guess of the frequency is close to the global minimum. In the case of multiple damped sine waves, random sampling is adopted to ensure quasiconvexity. In the single damped sine wave case, simple method mentioned in the introduction are applicable [16]. As an alternative to the use of accelerometers to provide an initial guess of the eigenfrequencies, a CS-based framework (*i.e.,* exploiting the sparsity of the modal response in the frequency domain) can extract it directly from the randomly sampled displacements. However, the state-of-the-art in modal analysis mostly adopts Fourier basis functions [38], which are not suited for damped structures, resulting in an incomplete set of initial guesses. Nonetheless, we see the potential of CS to avoid the need of having an accelerometer, and in future work we will investigate the use of different basis functions.

Table 1: Simulation setup (base case).

Name	Value
Number of waves	20
Frequency	$1\,\mathrm{Hz}$ to $500\,\mathrm{Hz}$
Damping	1×10^{-3} to 1
Amplitude	$1 \times 10^{-4}\,\mathrm{mm}$ to $1\,\mathrm{mm}$
Phase	0 to 2π rad
SNR (Signal-to-Noise Ratio)	$20\,\mathrm{dB}$
Frame rate	$< 100\,\mathrm{fps}$
Time interval	$0.01\,\mathrm{s}$ to $0.02\,\mathrm{s}$
Measurement time	$\sim 6\,\mathrm{s}$
Number of time samples	400

4. Numerical validation of the proposed approach

To assess the proposed methodology numerically, displacements are simulated by a combination of damped sine waves. In this section we present the simulation setup in section 4.1, we discuss the simulation results in section 4.2, and finally we analyze the influence of the amount of modes in section 4.3.

4.1. Simulation setup

As stated in section 3.1, there is a minimum to the sampling time interval. In the simulation, we set $\Delta t_{min} = 0.01\,\mathrm{s}$, and the time interval is thus randomly selected from $0.01\,\mathrm{s}$ to $0.02\,\mathrm{s}$. The simulated damped sine waves are $\sum_{i=1}^{N} \Re(A_i e^{\lambda_i t})$, where $A_i = a_i e^{j\varphi_i}$ and $\lambda_i = 2\pi f_i j - \sigma_i$. Among these predefined parameters, the frequency f_i and phase φ_i are randomly selected and their ranges are listed in table 1. The damping σ_i and amplitude a_i are represented in scientific notation, *i.e.*, $p \times 10^q$, where p, q are selected randomly. Noise is added to the modal response and its maximum amplitude is one-tenth of the minimum amplitude of the sine waves, resulting in a $20\,\mathrm{dB}$ signal-to-noise ratio.

With these parameters we have generated a set of randomly sampled damped sine waves, and we have verified that the optimization model in eq. (5) can recover the complete signal. The highest frequency of the displacement to be reconstructed is approximately $500\,\mathrm{Hz}$, and consequently the sampling frequency should be at least $1000\,\mathrm{Hz}$ with a regular sampling. However, the equivalent sampling frequency (expected number of captured frames in one second) in case of the proposed random sampling scheme is less than $100\,\mathrm{Hz}$, *i.e.*, approximately $1/10$ of the required (regular) sampling frequency.

To simulate a realistic error of the eigenfrequencies calculated with the accelerometer data, we shifted the target frequencies by $0.05\,\mathrm{Hz}$ to be used as initial guesses, while the frequency bound $\Delta\gamma_i$ in eq. (8) is $0.09\,\mathrm{Hz}$ around those frequencies. Finally, we set the lower bound of the damping values to zero, as damping factors are always positive.

4.2. Simulation results

For the considered numerical example, the accuracy of the optimization, indicated by the Mean Squared Error (MSE) over the time samples, is $6.74 \times 10^{-12}\,\mathrm{mm}^2$, which is lower than the squared amplitude of all damped sine waves, and thus the recovered signal overlaps well with the original signal as fig. 8(a) shows in the frequency domain.

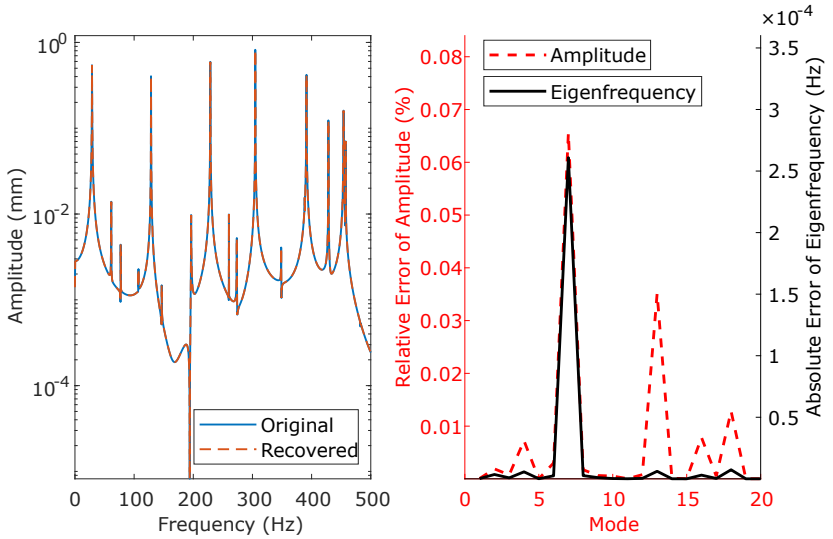

(a) Signal in frequency domain (b) Error of the recovered amplitude and frequency

Figure 8: Simulation error for the 20 components.

In time domain, thanks to the optimized signal parameters we recovered the regularly sampled response with the sampling frequency $1 \times 10^4\,\mathrm{Hz}$ and the measurement time $5\,\mathrm{s}$. Compared with the original signal generated from predefined variables, the overall MSE of recovered signal over time is $2.63 \times 10^{-11}\,\mathrm{mm}^2$.

By comparing the estimated frequencies with the target values, we notice that the errors are lower than $3 \times 10^{-4}\,\mathrm{Hz}$ as fig. 8(b) indicates. Similarly to the Non-Harmonic Fourier Analysis (NHFA) [54], the recovered signal from the proposed nonlinear optimization is not affected by spectral leakage, and the accuracy of frequency depends on the parameter estimation. However, the amplitudes cannot be directly compared because of the presence of damping. Performing the Fourier transform on the recovered signal, we can evaluate the accuracy of the recovered amplitudes in the frequency domain by deviation from their predefined values in table 1. We notice that the highest relative error occurs at the 7^{th} component (0.065%) as shown in fig. 8(b), which is the lowest peak in the frequency spectrum ($2.48 \times 10^{-4}\,\mathrm{mm}$). Therefore, given the simulated SNR of $20\,\mathrm{dB}$, we conclude that the nonlinear optimization did recover the correct signal.

4.3. Influence of the number of modes

As the frequency range of interest of a certain application may include several relevant modes, in this section we analyze the influence of the number of modes on the accuracy of

the reconstructed signal. To this purpose, we randomly generated the parameters of 100 damped sine waves. Starting from 5 modes, we gradually appended more modes to the starting modal response, and calculated the MSE of both the curve fitting with randomly sampled time instances and of the recovered signal with (high frequency) regular sampling.

As fig. 9 shows, when increasing the number of modes the MSE increases. When the number of modes exceeds 100, the optimization becomes an underdetermined problem, given that 4 unknown variables exist in one damped sine wave, and there are only 400 samples in time. In addition, the damping leads to correlated damped sine waves, and consequently the error of the recovered signal becomes large when the number of mode approaches 100, starting already around 60 whose MSE of the recovered signal is $6.58 \times 10^{-8}\,\mathrm{mm}^2$.

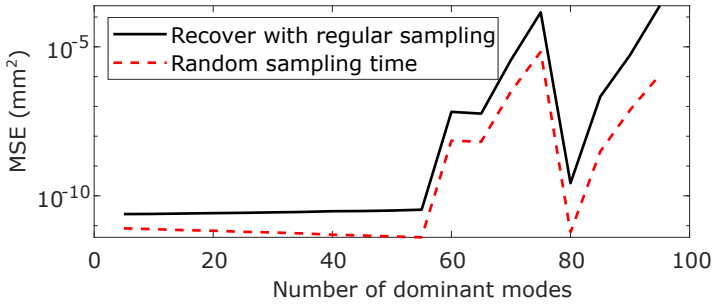

Figure 9: Error of curve fitting at randomly sampled time instances and the recovered complete signal when increasing the number of modes.

Finally, our simulation indicated that it is of paramount importance that the accelerometer provides a starting value for every modes of interest, *i.e.*, omitting a mode results in an error, whereas including extra (wrong) modes does not jeopardize the results, as it is barely noticeable in the reconstructed signal. Compared with the CS-based frameworks, accelerometer based selection is more straightforward, hence the latter is more advantageous in this case.

5. Experimental validation

To test experimentally the proposed methodology, we performed a camera-based EMA on an aluminum beam [55]. In this section, the experimental setup is described in section 5.1. Section 5.2 illustrates the procedure of recovering the modes from a randomly captured video, and finally section 5.3 discusses the recovered modes to validate the proposed approach.

5.1. Experimental setup

The beam is mounted to two vertical mounts in a clamped-clamped configuration. Two accelerometers (cf. fig. 12) are mounted on the beam to measure the eigenfrequencies. Theoretically one accelerometer is sufficient, but a redundant one avoids missing eigenfrequencies in case the accelerometer would be positioned at a modal node. Vibration of the beam is captured by a single camera as shown in fig. 4. The camera used in the experiment is a Ximea xiB-64 CB120RG-CM-X8G3 [56]. With regular sampling, its maximum frame rate is 66 fps at full

resolution (4096×3072 pixels) and full bit depth ($12\,\mathrm{bit}$). As the length of the beam is $1\,\mathrm{m}$, the resulting resolution is $3332\,\mathrm{pixel/m}$. A higher frame rate can be obtained by reducing the spatial resolution, as the bottle neck is the data transfer rate, but by doing so the displacement accuracy decreases. The camera is triggered by the rising edge of a square wave, whose time interval is randomly selected from $0.02\,\mathrm{s}$ to $0.04\,\mathrm{s}$ (cf. fig. 10), and the equivalent frame rate is less than $50\,\mathrm{fps}$.

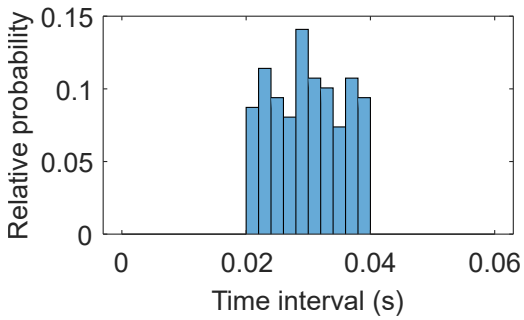

Figure 10: Probability of the time intervals between trigger pulses.

The bit depth of the images is set to $12\,\mathrm{bit}$ to reduce the Intensity Discretization Bias (IDB) in comparison with $8\,\mathrm{bit}$. The IDB is due to the quantization of the gray level intensity values in the digital camera, and it was found experimentally in [27] that the IDB of an 8-bit image set is 100 times the IDB of a 12-bit set (*i.e.*, 10^{-5}). 8-bit image set is acceptable if its IDB and noise level do not increase the residual considerably during the optimization.

The exposure time was set as $0.001\,\mathrm{s}$. This value is feasible from a hardware point of view, and it is short enough to have sufficient brightness, SNR (in general, reducing exposure time prevents the oversaturation of pixels and motion blur, but the captured image will have a low brightness level and a low SNR especially under scarce illumination [57]), and finally to capture the targeted frequency range (as an increased exposure time acts as low-pass filter [28]).

As introduced in section 2.2, eq. (4) of the LK optical flow indicates that an accurate tracking requires a sharp spatial gradient in gray level. Therefore, on the beam we have attached some high-contrast checkerboard markers, otherwise the number of sharp corners on the beam is not sufficient for the displacement measurement.

5.2. Workflow

The workflow from image acquisition to EMA is illustrated in fig. 11, and is discussed in the following list:

(a) We randomly trigger the camera and capture a video of the vibrating beam after a hammer hit.

(b) Using the first frame of the video as the reference image, we extract the corner points. These are fitted by a cubic function to remove the points located in the background. We track the 1D mesh points on the cubic curve by the LK optical flow, and the number of points is approximately 1×3000 as shown in fig. 12. We extract the y-axis (vertical) displacements of the mesh points, apply a median filter to the displacements and average displacements to reduce noise and obtain displacements of 500 points (fig. 13).

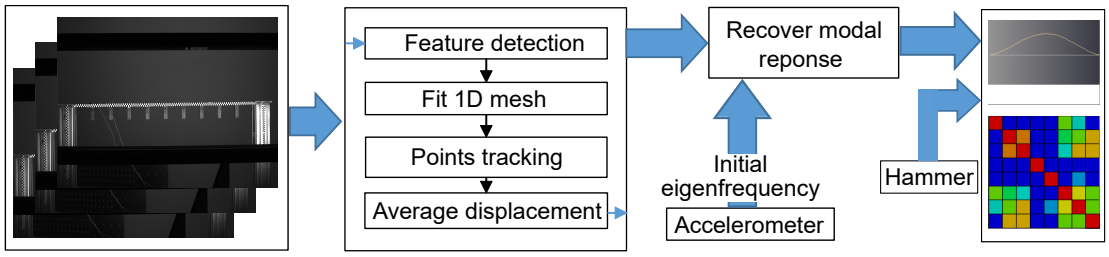

(a) Randomly sampled images (b) Displacement measurement (c) Nonlinear optimization (d) EMA

Figure 11: Data processing procedure.

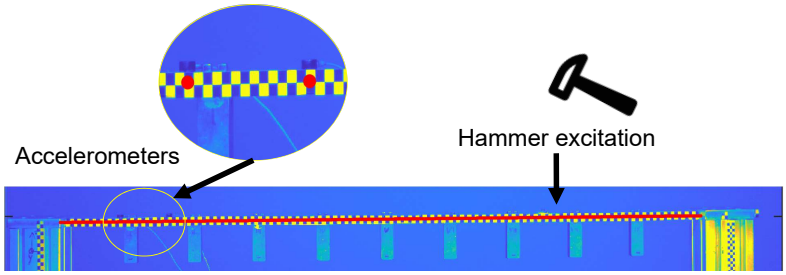

Figure 12: 1D mesh (red line) on the beam.

(c) To obtain the initial guess of the eigenfrequencies, we measure the acceleration response using accelerometers (fig. 16(a)). Afterward we apply PolyMAX partially on the acceleration to automatically select eigenfrequencies [48]. There are 8 dominant modes below 500Hz observed from the acceleration, *i.e.*, 25.575, 63.595, 73.013, 134.825, 218.373, 316.289, 397.041, and 428.231 (Hz). The frequency bound $\Delta\gamma_i$ in eq. (8) is set to the resolution of the accelerometers, *i.e.*, 0.09 Hz. With the initial guess and bound, we optimize eq. (8) and obtain frequency, damping, amplitude, and phase of the modal response (fig. 14).

(d) Finally, we recover the displacements by using the estimated parameters with higher sampling frequency, allowing us to obtain the mode shapes of the beam through PolyMAX [45] (fig. 15).

In step (b) we mentioned that we set the first frame as a static reference image. This is acceptable for the low amplitude displacements of our experiment. The tracking error would accumulate if we update the reference image at every step, *i.e.*, considering the first frame between every two consecutive frames as the reference image. In the case of higher amplitude, the coarse-to-fine estimation with a multi-level of the image pyramid can be applied.

The feature point detection is achieved by the minimum eigenvalue algorithm [49], which is simple and suitable for LK optical flow algorithm. During detection, if the eigenvalues of an image subset in two directions are all higher than a prescribed threshold, the image subset contains a sharp corner or salt-and-pepper textures, both of which can be tracked well by the LK optical flow.

To remove any feature points related to the background, we fitted a 1D mesh on these corner points to track in step (b). The points in the 1D mesh are close to the detected points by the

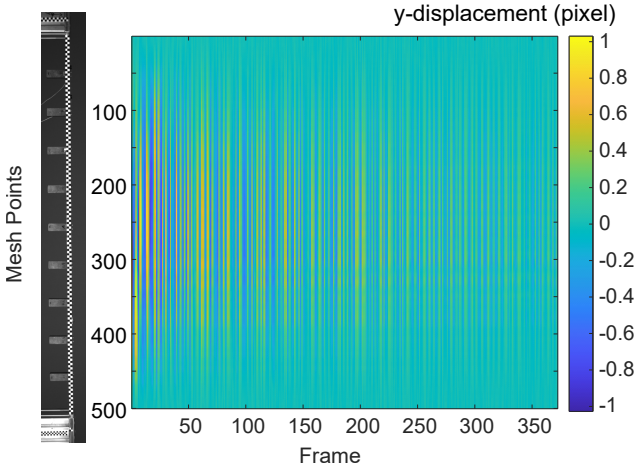

Figure 13: Measured displacements of the 500 feature points.

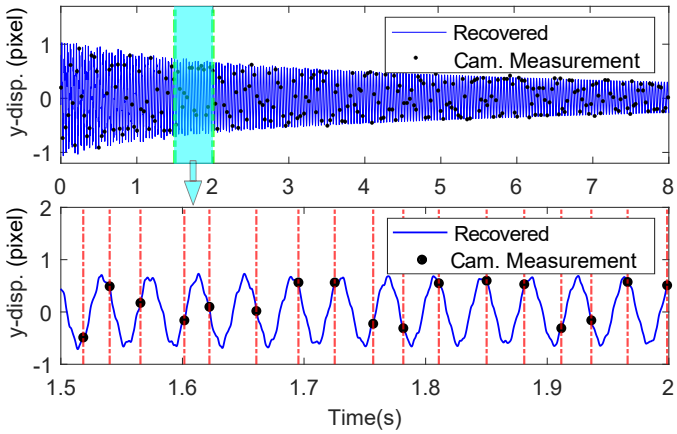

Figure 14: Curve fitting of measured y-displacements by the camera.

minimum eigenvalue algorithm, and an image subset around them will contains both of them, hence the LK optical flow (as a subset-based tracking algorithm) can track the subset around the 1D mesh successfully. In the beam's case, we used the *a priori* knowledge of the beam's geometry to remove the feature points in the background, and the general procedure is shown in fig. 4, where we can also remove irrelevant feature points or manually delete them by combining *a priori* knowledge (*e.g.,* a static background in comparison with the dynamic specimen) in the case of other specimens.

5.3. Experimental results

Dominated by the motion of the first mode, the measured displacement in fig. 13 has its largest value in the center of the beam. To calculate the noise level in the measurement, the relation between the standard deviation of the camera noise (std_{cam}) and the estimated displacement (std_y) is derived as $std_y^2 = (I_y^\top I_y)^{-1} std_{cam}^2$ [58]. In the experiment, $std_{cam} = 3$ in gray scale

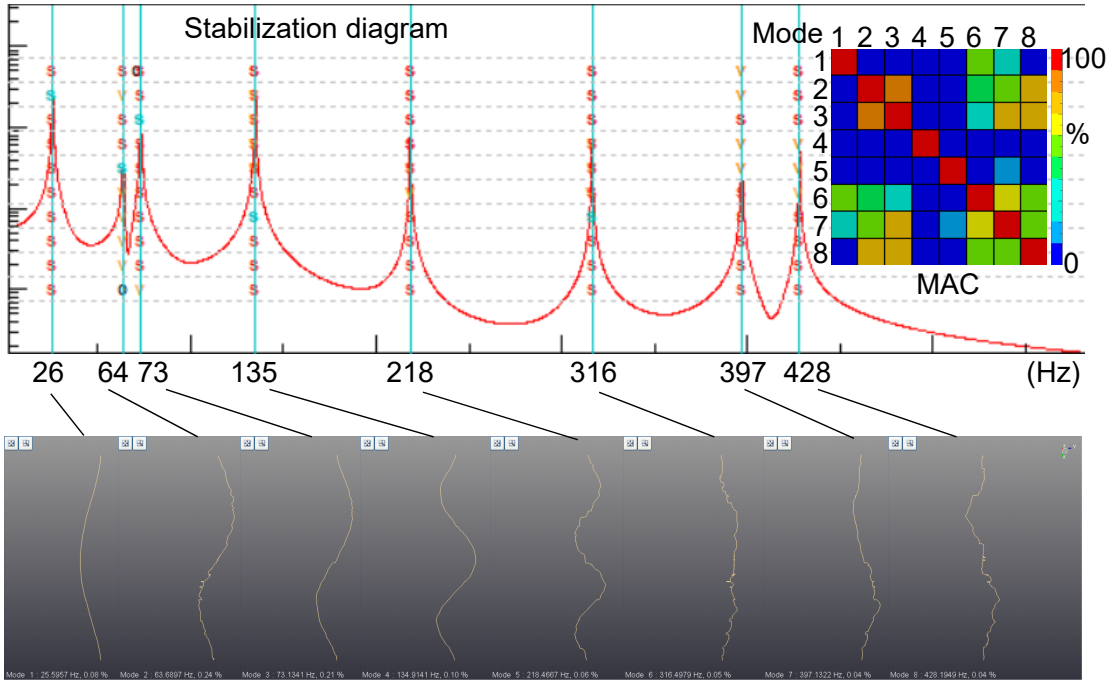

Figure 15: Stabilization diagram, MAC matrix and mode shapes.

values. With the highest spatial gradient (*i.e.*, 4096) for a 12 bit image, the smallest standard deviation of the displacement in the y direction (std_y) is 7.3×10^{-4} pixel, and $std_x = std_y$.

To compare our camera-based EMA with an accelerometer-based EMA, we integrate twice the accelerometer measurements (as mentioned in section 2.3) by $\mathcal{F}(x_{px}) = \beta\mathcal{F}(\alpha)/(j\omega)^2$ in the frequency domain, where $\beta = 3332\,\mathrm{pixel/m}$ is the spatial resolution of the images, and x_{px} is the displacement in pixel.

To evaluate the accuracy of the camera-based measurements, we focused on the displacement of two feature points located next to the two accelerometers (fig. 12). A comparison between the camera-based displacement and the first accelerometer shows that the peaks of the lowest 5 modes overlap well (fig. 16(a)), whereas the peaks of the highest 3 modes are below the noise level. The comparison with the second accelerometer also confirms that the highest 3 modes were not recovered successfully. The deviation of the measured modes between camera and accelerometers is in the range of 3×10^{-3} pixel (fig. 16(b)), which is higher than the amplitude of modes 6, 7 and 8. (The amplitudes of the measured signal at 427.8 Hz (mode 8) from accelerometer 1 and 2 are 9×10^{-4} pixel and 6×10^{-4} pixel, respectively, which are close to std_y and thus unidentifiable, as we can see in fig. 15). The noise is also the reason for stopping the eigenfrequency selection at mode 8, as peaks of higher modes are below std_y.

Due to the frequency bound $\Delta\gamma_i$ in eq. (8), the "S" points are aligned in the stabilization diagram fig. 15, indicating that the modes estimated by PolyMAX are stable [45].

The mode shapes in fig. 15 show that the first 5 modes match well the theoretical modes of a clamped-clamped beam. This is also verified by checking the complexity of the modes,

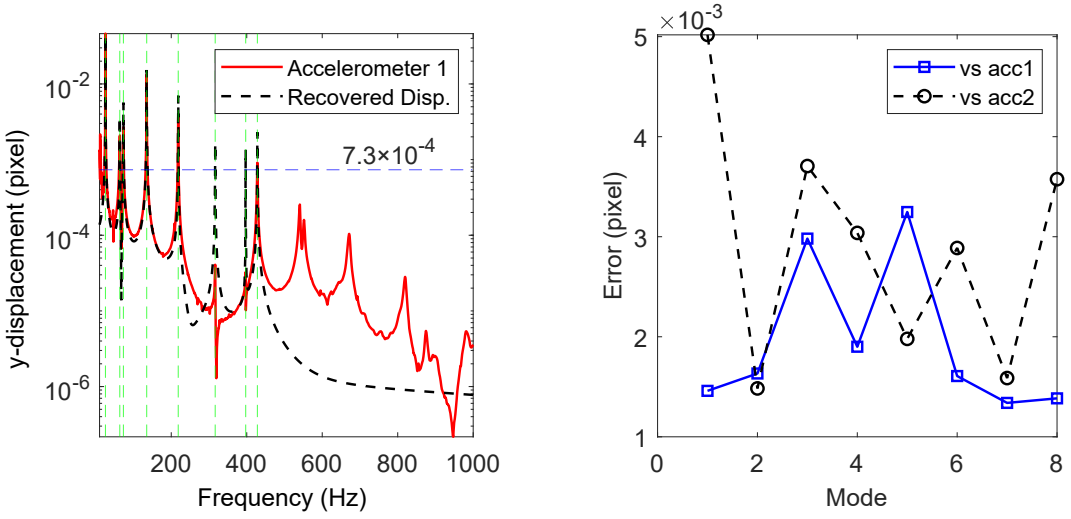

(a) Frequency spectrum

(b) Deviation

Figure 16: Comparison between displacements derived from accelerometer data and recovered from camera data.

indicated by the Mean Phase Deviation (MPD), the Modal Phase Collinearity (MPC) and the phase scatter, as table 2 shows. The modal response of a vibrating beam with no damping and no noise is a superposition of sine waves, and the phase and imaginary parts of the modes should be zero, *i.e.,* MPD is zero, MPC is 100% and there is no phase scatter. In our case, damping exists (due to energy loss through thermal effects and internal friction during deformation) but is rather low ($<1\%$), and thus the MPD and phase scatter are expected to be low while the MPC is expected to be high. According to these indicators, the mode shapes of modes 1 to 4 are real modes because of the low complexity (MPC$>95\%$ and MPD$<15°$), whereas modes 6 to 8 are not identifiable due to noise.

The Modal Assurance Criterion (MAC) can quantify the correlation among different mode shapes. If the weighted factors of the mass are evenly spread over the beam, the MAC matrix is diagonal, and the correlation among different mode shapes is zero. In the MAC matrix of the experiment (fig. 15) we can distinguish mode 5 by its low correlation with the other modes (close to 0%), although its complexity is higher than mode 1 to 4. The MAC of modes 2 and 3 also shows that the similarity of their correspondent mode shapes is high (almost 90%). The dynamical behavior of the experimental structure (*i.e.*, the beam) is described in detail in [59], where it becomes clear that the contribution of the vertical mounts is not negligible. Accordingly, it is possible that mode 2 relates to the vertical mounts. Nevertheless, the beam's vibration is dominant in the captured video.

6. Conclusions and next steps

In this paper, we proposed a methodology to go beyond the Nyquist-Shannon sampling frequency in the case of a camera-based EMA with impact excitation. This is achieved thanks to a random sampling scheme in time, one accelerometer and an optimization problem. Specifically,

Table 2: Modal validation.

Property	Frequency (Hz)	MPC (%)	MPD (°)	Phase scatter
Mode 1	25.595	99.963	0.604	low
Mode 2	63.678	95.578	13.509	low
Mode 3	73.054	99.370	6.482	low
Mode 4	134.914	99.750	2.962	low
Mode 5	218.418	91.827	26.884	?
Mode 6	316.384	28.621	37.185	high
Mode 7	397.011	89.210	26.227	high
Mode 8	428.198	90.132	25.444	?

we measured modes up to $218\,\mathrm{Hz}$ with a sampling scheme comparable to a regular sampling of $50\,\mathrm{fps}$. The nonlinear optimization is robust (*i.e.*, the global minimum of the error function is guaranteed) thanks to the data coming from an accelerometer providing an initial eigenfrequency value and a bound.

The modes obtained by the proposed approach have a high spatial resolution (500 points), without repetitions of the experiment. Furthermore, the number of images to be transferred and stored is lower in comparison to regular sampling. For the experiment discussed in this paper, the number of randomly triggered frames is 372 during a measurement period of $11\,\mathrm{s}$, whereas the same experiment would require approximately 4800 frames in case of the standard regular sampling respecting the Nyquist-Shannon sampling theorem.

In the camera measurements, the noise level is higher than that of accelerometer measurements. Averaging the camera data may reduce the noise as what conventional EMA employs, because FRFs in different experiments are correlated whereas the noise should not be correlated.

Although the proposed methodology is derived for (and applied to) an impact excitation, it is possible to extend it to other excitation types by substituting the excitation signal (*e.g.,* from a shaker) into the IRF model by convolution, followed by the A_i, and λ_i optimization as described in section 3. Furthermore, the proposed random sampling strategy can also be applied to OMA.

In the proposed approach, at least one accelerometer is needed to provide an initial guess of the eigenfrequencies. However, this information can potentially be extracted directly from the available camera-based displacement signals. To go in this direction, Compressive Sensing (CS) can be employed based on a well-chosen set of basis functions. The authors have performed a preliminary analysis where a few peaks could be retrieved from the randomly sampled displacement measurements via CS. However, the retrieved number of eigenfrequencies was not sufficient to replace the accelerometers yet. Nevertheless, we believe that by using a different set of basis functions together with an advanced solver we will be able to retrieve all eigenfrequencies. As such, this is a promising topic to be investigated in future research with the aim of making the approach completely contactless.

Finally, we will cope with rigid body motion by formulating it into the optimization model, to make the proposed methodology applicable to other boundary conditions in addition to the clamped-clamped condition.

Acknowledgments

The work leading to this publication has been funded by the ICON project"DETECT-ION", which fits in the MacroModelMat (M3) research program, coordinated by Siemens (Siemens Digital Industries Software, Belgium) and funded by SIM (Strategic Initiative Materials in Flanders) and VLAIO (Flemish government agency Flanders Innovation & Entrepreneurship). The Research Foundation – Flanders (FWO) is gratefully acknowledged for its support through research grant no. G095120N. The research was also funded by an Early Stage Researcher grant within the European Project ACOUTECT, Marie Curie Initial Training Network (GA 721536). Furthermore, Internal Funds KU Leuven are gratefully acknowledged for their support.

References

[1] W. Fan, P. Qiao, Vibration-based damage identification methods: A review and comparative study, Structural Health Monitoring: An International Journal 10 (1) (2010) 83–111. doi:10.1177/1475921710365419.

[2] S. Das, P. Saha, S. K. Patro, Vibration-based damage detection techniques used for health monitoring of structures: a review, Journal of Civil Structural Health Monitoring 6 (3) (2016) 477–507. doi:10.1007/s13349-016-0168-5.

[3] R. Brincker, C. Ventura, Introduction to operational modal analysis, John Wiley & Sons, 2015.

[4] M. D. Ulriksen, D. Tcherniak, P. H. Kirkegaard, L. Damkilde, Operational modal analysis and wavelet transformation for damage identification in wind turbine blades, Structural Health Monitoring: An International Journal 15 (4) (2016) 381–388. doi:10.1177/1475921715586623.

[5] P. Poozesh, J. Baqersad, C. Niezrecki, P. Avitabile, E. Harvey, R. Yarala, Large-area photogrammetry based testing of wind turbine blades, Mechanical Systems and Signal Processing 86 (2017) 98–115. doi:10.1016/j.ymssp.2016.07.021.

[6] Y. Yang, S. Nagarajaiah, Output-only modal identification by compressed sensing: Non-uniform low-rate random sampling, Mechanical Systems and Signal Processing 56-57 (2015) 15–34. doi:10.1016/j.ymssp.2014.10.015.

[7] E. Orlowitz, A. Brandt, Comparison of experimental and operational modal analysis on a laboratory test plate, Measurement 102 (2017) 121–130. doi:10.1016/j.measurement.2017.02.001.

[8] C. M. Pappalardo, D. Guida, System identification and experimental modal analysis of a frame structure., Engineering Letters 26 (1) (2018).

[9] A. Cusano, P. Capoluongo, S. Campopiano, A. Cutolo, M. Giordano, F. Felli, A. Paolozzi, M. Caponero, Experimental modal analysis of an aircraft model wing by embedded fiber bragg grating sensors, IEEE Sensors Journal 6 (1) (2006) 67–77. doi:10.1109/JSEN.2005.854152.

[10] D. M. Siringoringo, Y. Fujino, Noncontact operational modal analysis of structural members by laser doppler vibrometer, Computer-Aided Civil and Infrastructure Engineering 24 (4) (2009) 249–265. doi:10.1111/j.1467-8667.2008.00585.x.

[11] A. Zanarini, Full field optical measurements in experimental modal analysis and model updating, Journal of Sound and Vibration 442 (2019) 817–842. doi:10.1016/j.jsv.2018.09.048.

[12] T. Brox, C. Bregler, J. Malik, Large displacement optical flow, in: 2009 IEEE Conference on Computer Vision and Pattern Recognition, 2009, pp. 41–48. doi:10.1109/CVPR.2009.5206697.

[13] S. Ricco, C. Tomasi, Dense lagrangian motion estimation with occlusions, in: 2012 IEEE Conference on Computer Vision and Pattern Recognition, IEEE, 2012. doi:10.1109/cvpr.2012.6247877.

[14] N. Wadhwa, M. Rubinstein, F. Durand, W. T. Freeman, Phase-based video motion processing, ACM Transactions on Graphics 32 (4) (2013) 1–10. doi:10.1145/2461912.2461966.

[15] J. G. Chen, N. Wadhwa, Y.-J. Cha, F. Durand, W. T. Freeman, O. Buyukozturk, Modal identification of simple structures with high-speed video using motion magnification, Journal of Sound and Vibration 345 (2015) 58–71. doi:10.1016/j.jsv.2015.01.024.

[16] S. Barone, P. Neri, A. Paoli, A. V. Razionale, Low-frame-rate single camera system for 3d full-field high-frequency vibration measurements, Mechanical Systems and Signal Processing 123 (2019) 143–152. doi:10.1016/j.ymssp.2019.01.016.

[17] D. Fleet, Y. Weiss, Optical flow estimation, in: Handbook of mathematical models in computer vision, Springer, 2006, pp. 237–257.

[18] S. Baker, D. Scharstein, J. P. Lewis, S. Roth, M. J. Black, R. Szeliski, A database and evaluation methodology for optical flow, International Journal of Computer Vision 92 (1) (2010) 1–31. doi:10.1007/s11263-010-0390-2.

[19] J. Javh, J. Slavič, M. Boltežar, The subpixel resolution of optical-flow-based modal analysis, Mechanical Systems and Signal Processing 88 (2017) 89–99. doi:10.1016/j.ymssp.2016.11.009.

[20] Y. Yang, C. Dorn, T. Mancini, Z. Talken, G. Kenyon, C. Farrar, D. Mascareñas, Blind identification of full-field vibration modes from video measurements with phase-based video motion magnification, Mechanical Systems and Signal Processing 85 (2017) 567–590. doi:10.1016/j.ymssp.2016.08.041.

[21] J. Javh, J. Slavič, M. Boltežar, High frequency modal identification on noisy high-speed camera data, Mechanical Systems and Signal Processing 98 (2018) 344–351. doi:10.1016/j.ymssp.2017.05.008.

[22] T. Bregar, K. Zaletelj, G. Čepon, J. Slavič, M. Boltežar, Full-field FRF estimation from noisy high-speed-camera data using a dynamic substructuring approach, Mechanical Systems and Signal Processing 150 (2021) 107263. doi:10.1016/j.ymssp.2020.107263.

[23] W. Heylen, S. Lammens, P. Sas, et al., Modal analysis theory and testing, Vol. 200, Katholieke Universiteit Leuven Leuven, Belgium, 1997.

[24] F. G. Cervantes, L. Kumanchik, J. Pratt, J. M. Taylor, High sensitivity optomechanical reference accelerometer over 10 kHz, Applied Physics Letters 104 (22) (2014) 221111. doi:10.1063/1.4881936.

[25] S. Sony, S. Laventure, A. Sadhu, A literature review of next-generation smart sensing technology in structural health monitoring, Structural Control and Health Monitoring 26 (3) (2019) e2321. doi:10.1002/stc.2321.

[26] J. Baqersad, P. Poozesh, C. Niezrecki, P. Avitabile, Photogrammetry and optical methods in structural dynamics – a review, Mechanical Systems and Signal Processing 86 (2017) 17–34. doi:10.1016/j.ymssp.2016.02.011.

[27] S. S. Fayad, D. T. Seidl, P. L. Reu, Spatial DIC errors due to pattern-induced bias and grey level discretization, Experimental Mechanics 60 (2) (2019) 249–263. doi:10.1007/s11340-019-00553-9.

[28] P. L. Reu, D. P. Rohe, L. D. Jacobs, Comparison of DIC and LDV for practical vibration and modal measurements, Mechanical Systems and Signal Processing 86 (2017) 2–16. doi:10.1016/j.ymssp.2016.02.006.

[29] H. André, Q. Leclère, D. Anastasio, Y. Benaïcha, K. Billon, M. Birem, F. Bonnardot, Z. Chin, F. Combet, P. Daems, A. Daga, R. D. Geest, B. Elyousfi, J. Griffaton, K. Gryllias, Y. Hawwari, J. Helsen, F. Lacaze, L. Laroche, X. Li, C. Liu, A. Mauricio, A. Melot, A. Ompusunggu, G. Paillot, S. Passos, C. Peeters, M. Perez, J. Qi, E. Sierra-Alonso, W. Smith, X. Thomas, Using a smartphone camera to analyse rotating and vibrating systems: Feedback on the SURVISHNO 2019 contest, Mechanical Systems and Signal Processing 154 (2021) 107553. doi:10.1016/j.ymssp.2020.107553.

[30] B. Martinez, A. Green, M. F. Silva, Y. Yang, D. Mascareñas, Sparse and random sampling techniques for high-resolution, full-field, BSS-based structural dynamics identification from video, Sensors 20 (12) (2020) 3526. doi:10.3390/s20123526.

[31] K. Gkoktsi, A. Giaralis, A multi-sensor sub-nyquist power spectrum blind sampling approach for low-power wireless sensors in operational modal analysis applications, Mechanical Systems and Signal Processing 116 (2019) 879–899. doi:10.1016/j.ymssp.2018.06.049.

[32] S. Li, D. Yang, G. Tang, M. B. Wakin, Atomic norm minimization for modal analysis from random and compressed samples, IEEE Transactions on Signal Processing 66 (7) (2018) 1817–1831. doi:10.1109/tsp.2018.2793907.

[33] Z. Yang, L. Xie, Exact joint sparse frequency recovery via optimization methods, IEEE Transactions on Signal Processing 64 (19) (2016) 5145–5157. doi:10.1109/tsp.2016.2576422.

[34] J. Y. Park, M. B. Wakin, A. C. Gilbert, Modal analysis with compressive measurements, IEEE Transactions on Signal Processing 62 (7) (2014) 1655–1670. doi:10.1109/tsp.2014.2302736.

[35] E. J. Candès, J. K. Romberg, T. Tao, Stable signal recovery from incomplete and inaccurate measurements, Communications on Pure and Applied Mathematics 59 (8) (2006) 1207–1223. doi:10.1002/cpa.20124.

[36] S. Ji, Y. Xue, L. Carin, Bayesian compressive sensing, IEEE Transactions on Signal Processing 56 (6) (2008) 2346–2356. doi:10.1109/tsp.2007.914345.

[37] M. F. Duarte, Y. C. Eldar, Structured compressed sensing: From theory to applications, IEEE Transactions on Signal Processing 59 (9) (2011) 4053–4085. doi:10.1109/tsp.2011.2161982.

[38] R. Klis, E. N. Chatzi, Vibration monitoring via spectro-temporal compressive sensing for wireless sensor networks, Structure and Infrastructure Engineering 13 (1) (2016) 195–209. doi:10.1080/15732479.2016.1198395.

[39] Y. Bao, Z. Shi, X. Wang, H. Li, Compressive sensing of wireless sensors based on group sparse optimization for structural health monitoring, Structural Health Monitoring 17 (4) (2017) 823–836. doi:10.1177/1475921717721457.

[40] R. Baraniuk, Compressive sensing [lecture notes], IEEE Signal Processing Magazine 24 (4) (2007) 118–121. doi:10.1109/msp.2007.4286571.

[41] J. Wang, S. Kwon, P. Li, B. Shim, Recovery of sparse signals via generalized orthogonal matching pursuit: A new analysis, IEEE Transactions on Signal Processing 64 (4) (2016) 1076–1089. doi:10.1109/tsp.2015.2498132.

[42] J. Javh, M. Brumat, J. Slavič, M. Boltežar, A high-speed camera measurement set-up for deflection shape analysis, Proceeding of ISMA2016-USD2016 (2016) 1043–1050.

[43] Y. Liu, H. Gao, J. Zhuge, J. Zhao, Research of under-sampling technique for digital image correlation in vibration measurement, in: Shock & Vibration, Aircraft/Aerospace, Energy Harvesting, Acoustics & Optics, Volume 9, Springer International Publishing, 2017, pp. 49–58. doi:10.1007/978-3-319-54735-0_6.

[44] J. Javh, J. Slavič, M. Boltežar, Measuring full-field displacement spectral components using photographs taken with a DSLR camera via an analogue fourier integral, Mechanical Systems and Signal Processing 100 (2018) 17–27. doi:10.1016/j.ymssp.2017.07.024.

[45] B. Peeters, H. Van der Auweraer, P. Guillaume, J. Leuridan, The polymax frequency-domain method: a new standard for modal parameter estimation?, Shock and Vibration 11 (3, 4) (2004) 395–409.

[46] P. Verboven, Frequency-domain system identification for modal analysis, Vrije Universiteit Brussel, Brussels (2002).

[47] R. A. de Callafon, D. de Roover, P. M. J. Van den Hof, Multivariable least squares frequency domain identification using polynomial matrix fraction descriptions, in: Proceedings of 35th IEEE Conference on Decision and Control, Vol. 2, 1996, pp. 2030–2035 vol.2. doi:10.1109/CDC.1996.572883.

[48] J. Lanslots, B. Rodiers, B. Peeters, Automated pole-selection: proof-of-concept and validation, in: Proceedings, International Conference on Noise and Vibration Engineering (ISMA), Citeseer, 2004.

[49] J. Shi, Tomasi, Good features to track, in: Proceedings of IEEE Conference on Computer Vision and Pattern Recognition CVPR-94, IEEE Comput. Soc. Press, 1994. doi:10.1109/cvpr.1994.323794.

[50] Z. Zhang, Flexible camera calibration by viewing a plane from unknown orientations, in: Proceedings of the seventh ieee international conference on computer vision, Vol. 1, Ieee, 1999, pp. 666–673.

[51] Z. Beheshti, S. M. H. Shamsuddin, A review of population-based meta-heuristic algorithms, Int. J. Adv. Soft Comput. Appl 5 (1) (2013) 1–35.

[52] S. Boyd, S. P. Boyd, L. Vandenberghe, Convex optimization, Cambridge university press, 2004.

[53] J. J. Moré, D. C. Sorensen, Computing a trust region step, SIAM Journal on scientific and statistical computing 4 (3) (1983) 553–572.

[54] P. Neri, B. Peeters, Non-harmonic fourier analysis for bladed wheels damage detection, Journal of Sound and Vibration 356 (2015) 181–194. doi:10.1016/j.jsv.2015.06.048.

[55] M. Kirchner, J. Croes, F. Cosco, B. Pluymers, W. Desmet, Compressive sensing-moving horizon estimator for periodic loads: experimental validation in structural dynamics with video-based measurements, Desmet, Wim, KU Leuven; Leuven, 2018, pp. 1487–1502.

[56] Ximea-cb120cg-cm-x8g3, https://www.ximea.com/en/products, accessed: 2021-02-17.

[57] S. Negahdaripour, Revised definition of optical flow: Integration of radiometric and geometric cues for dynamic scene analysis, IEEE Transactions on Pattern Analysis and Machine Intelligence 20 (9) (1998) 961–979.

[58] Y. Wang, P. Lava, P. Reu, D. Debruyne, Theoretical analysis on the measurement errors of local 2d DIC: Part i temporal and spatial uncertainty quantification of displacement measurements, Strain 52 (2) (2015) 110–128. doi:10.1111/str.12173.

[59] M. Kirchner, Joint state/input estimation in structural dynamics-state/force estimation using compressive sensing within a multistep approach (2018).